Supplementary Information Manuscript

$BaCe_{0.25}Mn_{0.75}O_{3-\delta}$ — A promising perovskite-type oxide for solar thermochemical hydrogen production

Debora R. Barcellos, Michael Sanders, Jianhua Tong[□], Anthony H. McDaniel[□], Ryan O'Hayre

Colorado School of Mines, Department of Metallurgical and Materials Engineering, Golden, CO, USA

[□]Clemson University, Clemson, Materials Science and Engineering, SC, USA

[□]Sandia National Laboratories, Combustion Research Facility, Livermore, CA, USA

Theoretical bond strength analysis

The E_v values provided in Table 1 column 3 were calculated according to Deml's[1] model equation:

$$E_V = 0.67\left[|\Delta H_f| + 0.6\left(E_{O\ 2p} + \frac{1.5}{2}E_g^{DFT+U}\right) + 2.6\langle\Delta\chi\rangle\right] - 1.49$$

where ΔH_f is the oxide formation enthalpy in eV/atom, $E_{O\ 2p}$ is the energy difference between the valence band maximum and the center of the O 2p band in eV (inferred from DOS diagrams reported in the literature), E_g^{DFT+U} is the calculated band gap in eV, and $\Delta\chi$ is the unitless average Pauling electronegativity difference between O atoms and the atoms forming their first coordination shell, meaning O electronegativity subtracted from Mn and Ce electronegativities. The quantities used for BMO and BCO are given in Table S1.

Table S1 – Reported calculated values used to approximate the oxygen vacancy formation energy

Compound	ΔH_f (eV/ atom)	$E_{O\ 2p}$ (eV)	E_g^{DFT+U} (eV)	$\Delta\chi$
$BaMnO_3$	2.0[2]	1.0[3]	1.6[3]	1.9
$BaCeO_3$	17.5[4]	0.8[5]	1.5[5]	2.3

X-ray diffraction analysis

Figure S1 demonstrates the XRD patterns obtained for the $BaCe_xMn_{1-x}O_3$ samples synthesized, where x = 0, 0.05, 0.15, 0.25, 0.50, 0.75 and 1 named respectively as BMO, BC05M95, BC15M85, BC25M75 (BCM), BC50M50, BC75M25 and BCO.

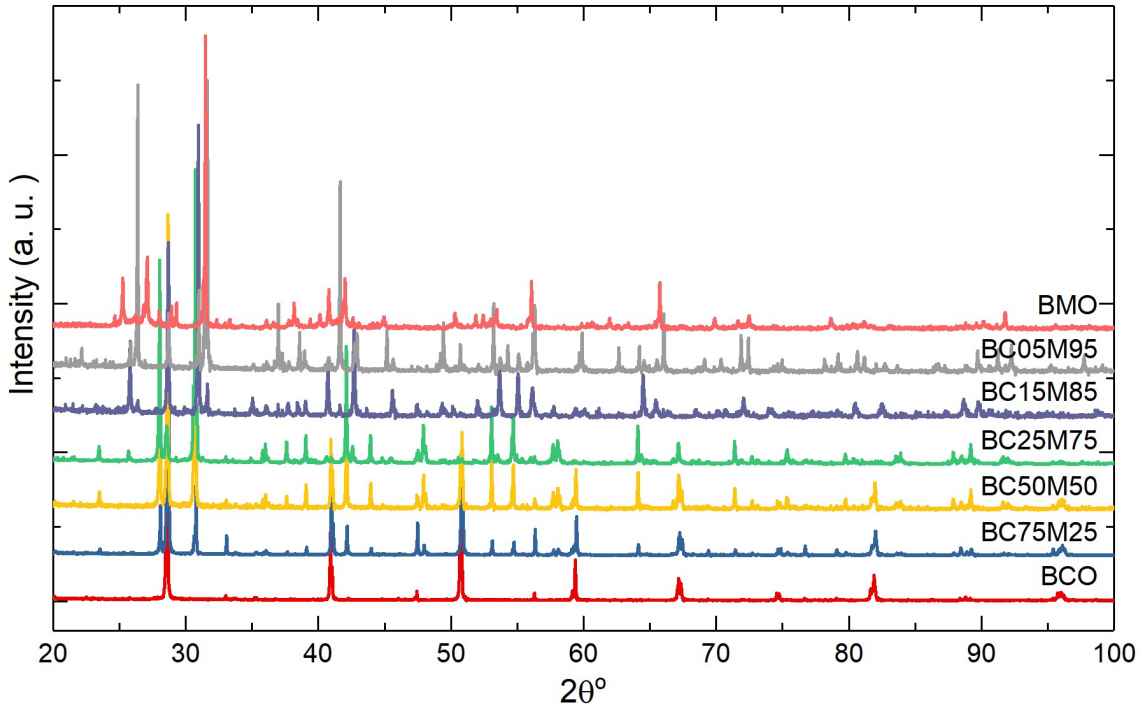

Figure S1 - X-ray diffraction comparison between the samples $BaCe_xMn_{1-x}O_3$, where x = 0, 0.05, 0.15, 0.25, 0.50, 0.75, and 1.

From the diffraction patterns, it can be noticed that the pure phase structures predicted could not be achieved, but instead a mixture of crystal structures compose most of the samples. It can also be noticed that the samples BC25M75, BC50M50 and BC75M25 have the phases $BaCe_{0.25}Mn_{0.75}O_{3-\delta}$ (R-3m), $BaCeO_3$ (Pnma) and CeO_2 (Fm-3m) in common. Rietveld refinement results are shown in Table S1. Rietveld Refinement quantification was not possible for samples BC05M95 and BC15M85 due to the multitude of secondary phases formed.

Table S2 - Crystal structures determined from Rietveld Refinement for each of the 5 samples studied.

Sample	**$BaCe_{0.25}Mn_{0.75}O_3$**	**$BaCeO_3$**	**CeO_2**	**$Ba_5Ce_{1.25}Mn_{3.75}O_{15}$**	**other**
Space Group (ICSD)	R-3m (166)	Pnma (62)	Fm-3m (225)	$P6_3/mmc$ (194)	-

BMO	-	-	-	-	58% $BaMnO_3$ R-3m (166) 28% $Ba_6Mn_5O_{16}$/ $Ba_4Mn_3O_{10}$ Cmca (64) 7% $BaMnO_3$ P63 mc (186) 7% Mn_3O_4 I41/amd (141)
BC25M75	83%	-	3%	14%	-
BC25M75 cycled	95%	3%	1%	1%	-
BC50M50	61%	36%	3%	-	-
BC75M25	28%	58%	14%	-	-
BCO	-	94%	6%	-	-

It is evident from the Rietveld refinement results that there is only one exact amount of Ce that can be added to the structure to form the Ce/Mn shared B-site layered perovskite, which is 0.25 mol of Ce and 0.75 mol of Mn.

This behavior was confirmed in the literature by Fuentes et al. It was indicated that although predictions suggest the potential occurrence of other amounts of Ce in the B-site, affecting the layering sequence, however no attempts to synthesize $BaCe_xMn_{1-x}O_3$ with different amounts of Ce were successful.

Macias et al. though were able to synthesize a polytype of the $BaCe_{0.25}Mn_{0.75}O_{3-\delta}$ (R-3m), identified as 10*H*-$Ba_5Ce_{1.25}Mn_{3.75}O_{15}$ (P63/mmc). This polytype has the same stoichiometric cation ratios Ba:Ce:Mn, respectively, 1:0.25:0.75, but has a difference in symmetry, forming a hexagonal structure. We were able to obtain this structure in very small quantity (14 %) in the BC25M75 sample. However, after one TPR cycle, (Figure S2), where the sample was reduced at a high temperature and then re-oxidized at a lower temperature, the polytype structure disappeared, forming a purer sample (95 % of the 12*R* structure with simple oxides as secondary phases).

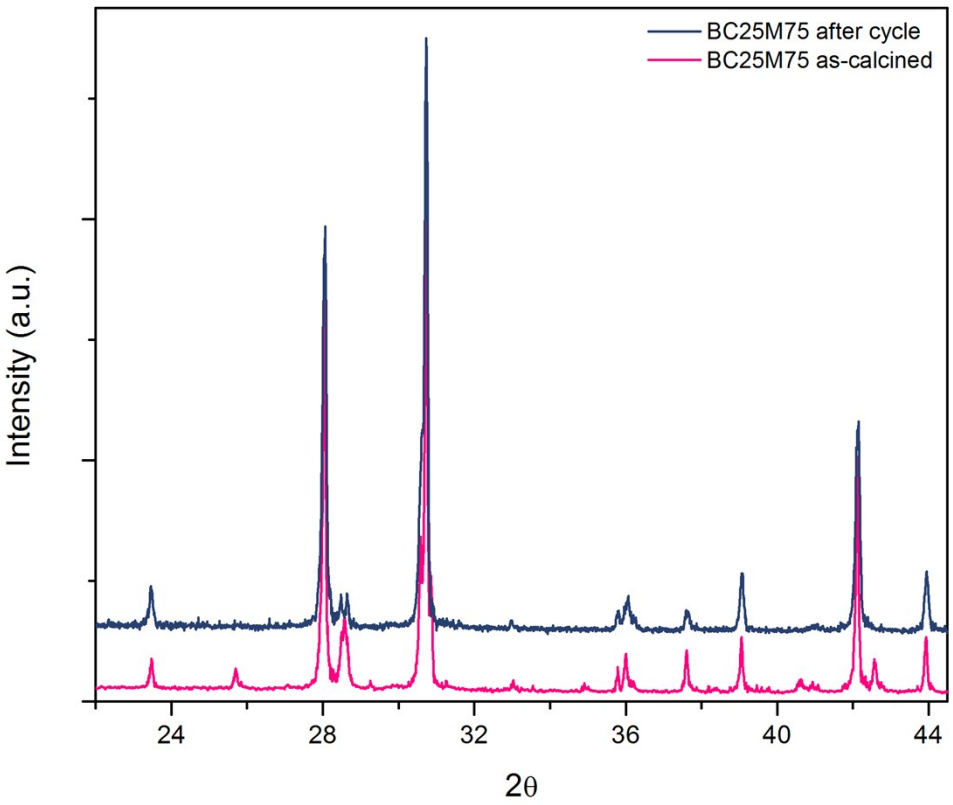

Figure S2 – X-ray diffraction results for BC25M75 sample as calcined and after the first TPR cycle (reduction at 1350 °C and re-oxidation at 1000 °C) shows the increase of the 12*R* structure and decrease of the 10*H* structure.

Temperature Programmed Reduction

The extent of the reduction, as well as the onset temperatures from the Temperature Programmed Reduction (TPR) experiment, are summarized on Table S3. The onset temperatures were obtained at the temperature where δ is equal to 0.025. The BC25M75 onset temperature is similar to SLMA, but lower than ceria.

Table S3 - Extent of reduction and onset temperature at δ = 0.025. Data obtained from TPR experiment where T_{RE} 1350 °C at 10 °C/min and held for 4 h and T_{OX} 1000 °C.

	Extent of reduction (mol O/ mol sample) or (δ)	Onset Temperature (°C) at δ = 0.025
Ceria	0.049	1270
BCO	0.039	900

SLMA	0.088	1230
BC75M25	0.157	620
BC50M50	0.103	1300
BCM	0.182	850
BC15M85	0.227	1200
BC05M95	0.345	950
BMO	0.424	790

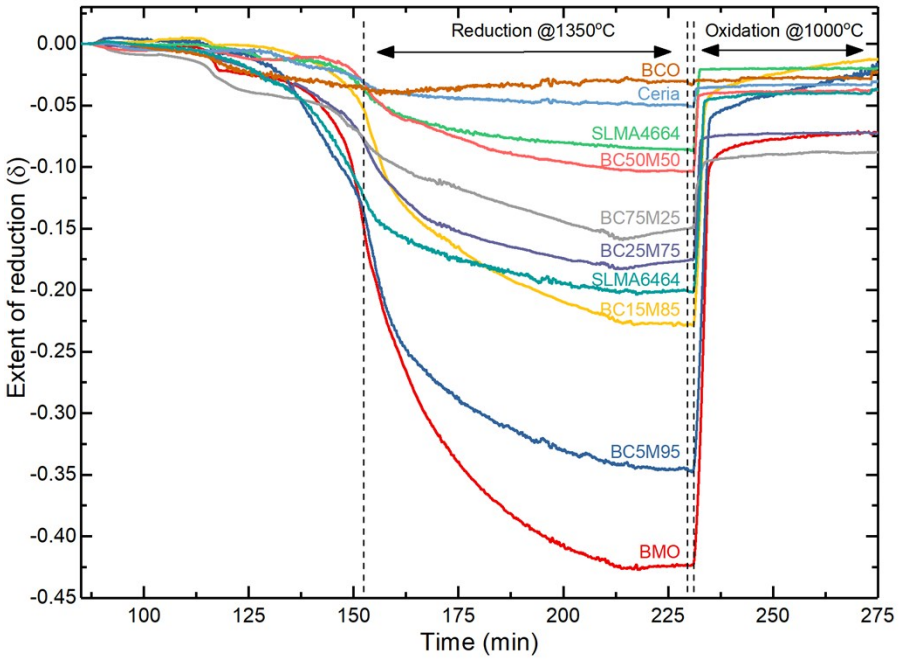

Figure S3 – Temperature Programmed Reduction experiment evaluates the extent of reduction (formation of oxygen vacancies or δ) and reversibility of samples BCO, ceria, SLMA, BC75M25, BC50M50, BC25M75, BC15M85, BC05M95 and BMO. Reduction at 1350 °C for 1 h in UHP N_2 and Oxidation in air at 1000 °C.

The compositions between BCO and BMO generally follow the trend of manganese rich phases reducing further than ceria rich phases, though the BC75M25 and BC50M50 positions reverse. This trend would likely be expected to hold if all compositions were single phase "alloys" of the two end members, but since the compositions are mixed-phase, the deviations should perhaps be unsurprising.

TPR was performed on the BCM sample, where three consecutive reduction (1350 °C) and oxidation (1000 °C) cycles are shown in Figure S4.

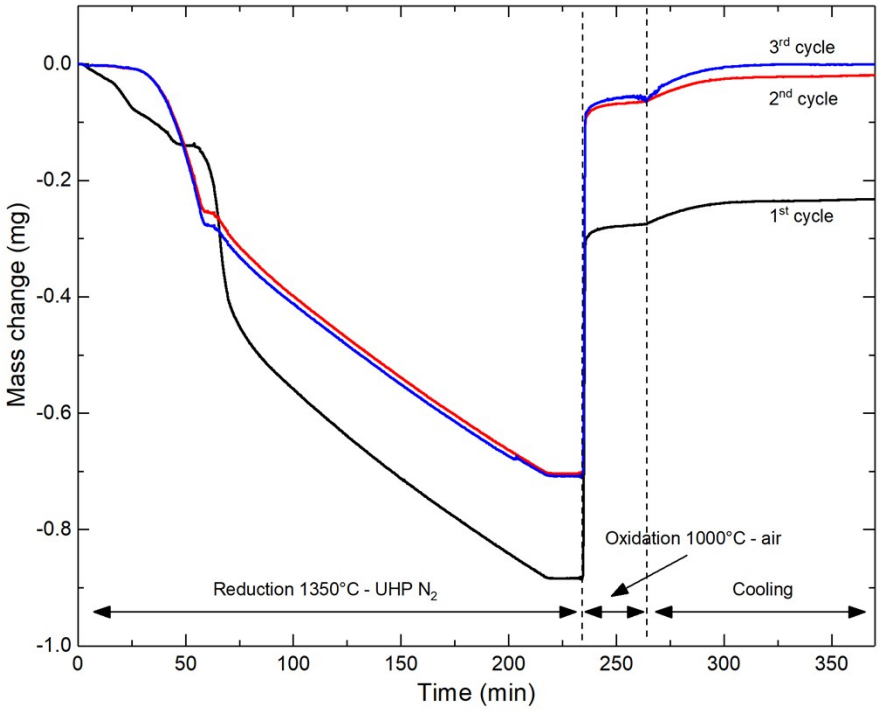

Figure S4 – BCM three consecutive reduction and oxidation cycles at 1350 °C in UHP N_2 for 4 h and 1000 °C for 30 min in air respectively. The experiment indicates that after the first redox cycle BCM two polytypes were all converted to the main phase 12*R*.

Figure S4 suggests that the first BCM cycle reduces to a higher extent and doesn't completely recover its mass. However, upon further cycling the sample demonstrates complete redox reversibility. This behavior might be attributed to the 10*H* secondary phase conversion to 12*R* primary phase, as shown by XRD.

Water-splitting experiments using Stagnation Flow Reactor

The three samples BC25M75 (BCM), SLMA and ceria (powder samples of surface area 0.20 m^2/g, 0.99 m^2/g and 2.24 m^2/g respectively) were tested for water splitting under various T_{OX} and T_{RE} conditions. The experiment was accomplished at Sandia in the Stagnation Flow Reactor (SFR) as described in the experimental section. Three oxidation temperatures and three reduction temperatures were probed maintaining the same reduction and oxidation times of 330 s and 20 min respectively, except for ceria where the oxidation hold time was only of 5 minutes. 40 vol. % of steam was used in all conditions. The average of the amounts of hydrogen produced per mass of material during each cycle is reported in Table S4 and plotted in Figure S5a and S5b.

Table S4- Hydrogen production (µmol/g of sample) at T_{OX} (750 °C, 850 °C and 1000 °C) and T_{RE} (1250 °C, 1350 °C) with 40 vol. % steam.

T_{OX} (°C)	Sample	T_{RE} (°C)		
		1250	**1350**	**1400**
750	BCM	52	99	136
	SLMA	74	150	205
	Ceria	28	46	67
850	BCM	56	139	165
	SLMA	89	194	256
	Ceria	26	50	68
1000	BCM	86	146	181
	SLMA	105	224	292
	Ceria	26	53	71

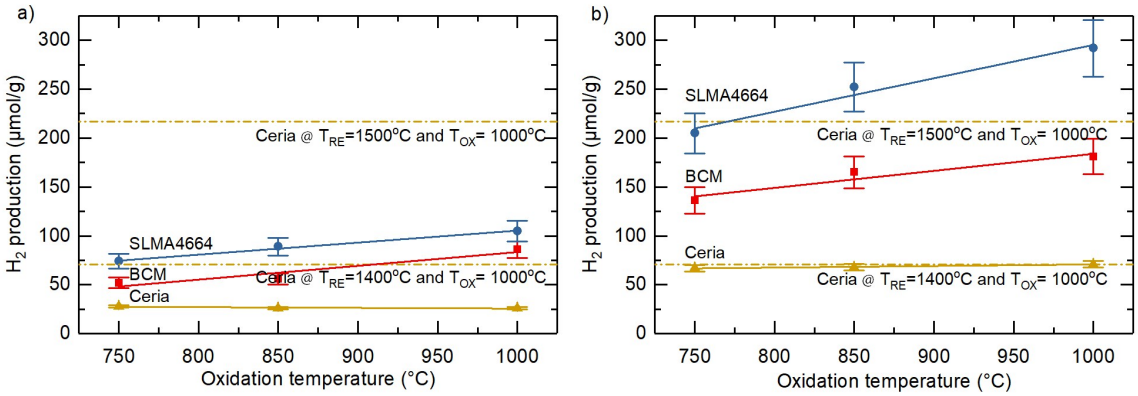

Figure S5 - Total H_2 produced per cycle by BCM (red), SLMA (blue) and Ceria (yellow) at a) T_{RE} of 1250 °C and b) T_{RE} of 1400 °C with 40% steam and various oxidation temperatures. Reduction heating rate is 10 °C/s, with a reduction time of 330 s and a reoxidation time of 1200 s.

In considering this comparative analysis of ceria, BCM, and SLMA4664, it should be noted that at T_{RE} 1350 °C and T_{OX} 1000 °C, we have previously reported per-cycle SLMA4664 H_2 production values significantly higher (as high as 277 µmol/g[11]) than those presented here. STCH H_2 yield is highly sensitive to cycle time. In the present analysis, we used a 330 s reduction time to better match realistic STCH reactor cycle durations. In our previous work, a reduction time of 1800 s was used,[11] which increases the extent of reduction and thus increases the measured water splitting capacity of the material.

In the main text, BCM's water splitting performance was compared to STCH 4664 and ceria under identical testing conditions. Direct comparison with other promising materials reported in the literature is not easy because of the diversity of cycle conditions used. A brief list of some of other promising materials for STCH reported in the literature can be found in Table S5 below.

Table S5 – Non-exhaustive list of promising STCH materials reported in the literature for comparison of performance.

Material	H_2 production (µmol/g)	Reduction step conditions	Oxidation step conditions
$BaCe_{0.25}Mn_{0.75}O_3$	140 (this work)	1350 °C for 330 s	850 °C for 1200 s – 40 vol% H_2O
CeO_2	220 (this work)	1500 °C for 330 s	1000 °C for 1200 s – 40 vol% H_2O
CeO_2	75 (this work)	1400 °C for 330 s	1000 °C for 1200 s – 40 vol% H_2O
CeO_2	50 (this work)	1350 °C for 330 s	850 °C for 1200 s – 40 vol% H_2O
$Ce_{0.75}Zr_{0.25}O_2$	354[6]	1400 °C for 45 min	1000 °C for 35 min – 80 % RH
$Ce_{0.75}Zr_{0.25}O_2$	162[7]	1450 °C for 45 min	950 °C for 25 min – 80 % RH
$Ce_{0.85}Fe_{0.15}O_2$	536[8]	1500 °C for 30 min	1150 °C for 30 min – pH_2O 0.5-0.84 atm
$Ce_{0.85}Co_{0.15}O_2$	768[8]	1500 °C for 30 min	1150 °C for 30 min – pH_2O 0.5-0.84 atm
$Ce_{0.85}Ni_{0.15}O_2$	688[8]	1500 °C for 30 min	1150 °C for 30 min – pH_2O 0.5-0.84 atm
$Ce_{0.85}Mn_{0.15}O_2$	491[8]	1500 °C for 30 min	1150 °C for 30 min – pH_2O 0.5-0.84 atm
$Sr_{0.4}La_{0.6}Mn_{0.6}Al_{0.4}O_3$	194 (this work)	1350 °C for 330 s	850 °C for 1200 s – 40 vol% H_2O
$Sr_{0.4}La_{0.6}Mn_{0.6}Al_{0.4}O_3$	307[9]	1350 °C for 30 min	1000 °C for 1000 s – 40 vol% H_2O
$Sr_{0.6}La_{0.4}Mn_{0.6}Al_{0.4}O_3$	277[9]	1350 °C for 30 min	1000 °C for 1000 s – 40 vol% H_2O
$Sr_{0.4}La_{0.6}Mn_{0.4}Al_{0.6}O_3$	220[9]	1350 °C for 30 min	1000 °C for 1000 s – 40 vol% H_2O
$CaTi_{0.7}Fe_{0.3}O_3$	39[9]	1400 °C for 30 min	1100 °C for 1000 s – 40 vol% H_2O
$(FeMgCoNi)O_x$	450[10]	1300 °C for 5 h	800 °C for 5 h – 9.5 vol% H_2O w/ 91 ppm H_2
$(FeMgCoNi)O_x$	150[10]	1300 °C for 30 min	800 °C for 1 h – 9.5 vol% H_2O w/ 91 ppm H_2

Numerical kinetics analysis

The kinetic behavior of the samples was analyzed by using a numerical approach developed by McDaniel et al. to separate the solid-state chemistry kinetic process from mainly three other events: 1- the time it takes for steam to enter the reactor, 2- the time lag of detection and 3- the dispersion effects of H_2 being produced and transported to the detector. A simulated oxidation experiment was performed where an empty zirconia boat was held at two oxidation temperatures 850 °C and 1000 °C. Instead of only steam, trace amounts of hydrogen in 40 vol. % steam where inserted in the reactor and detected in the mass spectrometer. The effects of the three events intrinsic to the experiment setup are then numerically determined by fitting a continuous stirred tank reactor (CSTR) model consisting, in this case of seven serial tanks to the resulting hydrogen signal. The fitted parameters for the reactor can then be applied to simple kinetic model curves, such as reaction-order, diffusion among other ones to produce simulated hydrogen production curves. Finally, using numerical methods, the kinetic model parameters are adjusted to fit the simulated curve to the actual experimental data and therefore extract the true rate-governing mechanisms in the materials such as surface reactions and bulk diffusion. The computational methods are discussed in further detail in McDaniel et al.[9] and Scheffe et al.[12]. Table S6 compiles the fitted parameters for the reactor using four blank runs.

Table S6 – Fitted parameters for the reactor calculated from four blank runs that used 2 sccm and 4 sccm trace amount of H_2 (5 % H_2 balanced in Ar) mixed in the 40 vol. % steam flow.

T_{OX} (°C)	Mixing model identification	Trace H_2 flow (sccm)	t_0 (s)	tau
850	M850-1	2	17.7	0.2617
	M850-2	2	20.7	0.2887
	M850-3	4	18.4	0.2740
	M850-4	4	19.2	0.2929
1000	M1000-1	2	19.0	0.2613
	M1000-2	2	16.2	0.2486
	M1000-3	4	17.5	0.2580
	M1000-4	4	18.2	0.2741

Tables S7 and S8 compile the calculated rate constants for each each material and condition using all the four mixing models. The r-square is also reported as an indication of fitting suitability. An average of the rate constants as well as the standard deviation for each T_{OX} condition and material is reported in the main manuscript.

Table S7- Rate constants calculated for BCM using the four different mixing models at 850 °C and 1000 °C.

T_{OX} (°C)	H_2 peak	Mixing model	k0	r-square
850	1st	M850-1	0.0132	0.9960
		M850-2	0.0131	0.9950
		M850-3	0.0121	0.9956
		M850-4	0.0130	0.9949
	2nd	M850-1	0.0129	0.9942
		M850-2	0.0128	0.9916
		M850-3	0.0128	0.9944
		M850-4	0.0127	0.9944
1000	1st	M1000-1	0.0168	0.9946
		M1000-2	0.0167	0.9980
		M1000-3	0.0168	0.9971
		M1000-4	0.0167	0.9974
	2nd	M1000-1	0.0157	0.9886
		M1000-2	0.0157	0.9943
		M1000-3	0.0158	0.9924
		M1000-4	0.0157	0.9933

Table S8- Rate constants calculated for ceria using the four different mixing models at 850 °C and 1000 °C.

T_{OX} (°C)	H2 peak	Mixing model	k0	r-square
850	1st	M850-1	0.1784	0.9858
		M850-2	0.1697	0.9693
		M850-3	0.1703	0.9892

		M850-4	0.1561	0.9915
	2nd	M850-1	0.2134	0.9935
		M850-2	0.2010	0.9792
		M850-3	0.1953	0.9936
		M850-4	0.1774	0.9937
1000	1st	M1000-1	0.0768	0.9705
		M1000-2	0.0764	0.9881
		M1000-3	0.0780	0.9836
		M1000-4	0.0756	0.984
	2nd	M1000-1	0.0744	0.9781
		M1000-2	0.0737	0.9915
		M1000-3	0.0759	0.9891
		M1000-4	0.0738	0.9896

To ensure that the WS results measured in this study could be fully attributed to the 12*R* phase, we conducted a simulated WS cycle on the 10*H* phase using TGA. We prepared a phase-pure 10*H* sample by reducing a BCM 12*R* sample for 24 h under UHP N_2 flow at 1350 °C. 50.3mg of 10*H* sample was loaded into a Pt crucible and heated under 100 sccm UHP N_2 at 10 °C/min to T_{OX} 850 °C. The reduction step was carried out heating the sample to TRE 1350 °C at 99°C/min (the fastest we could heat in the TGA to simulate the laser heating) and holding the temperature for 330 s. The sample was then cooled to T_{OX} at the same fast ramp rate and 16 sccm of synthetic air was flowed for 10 min to initiate oxidation. The synthetic air flow was turned off the and UHP N_2 gas was flowed for 10 min to purge the O_2 from the chamber before the subsequent reduction step. Figure S6 shows the TGA simulated run results.

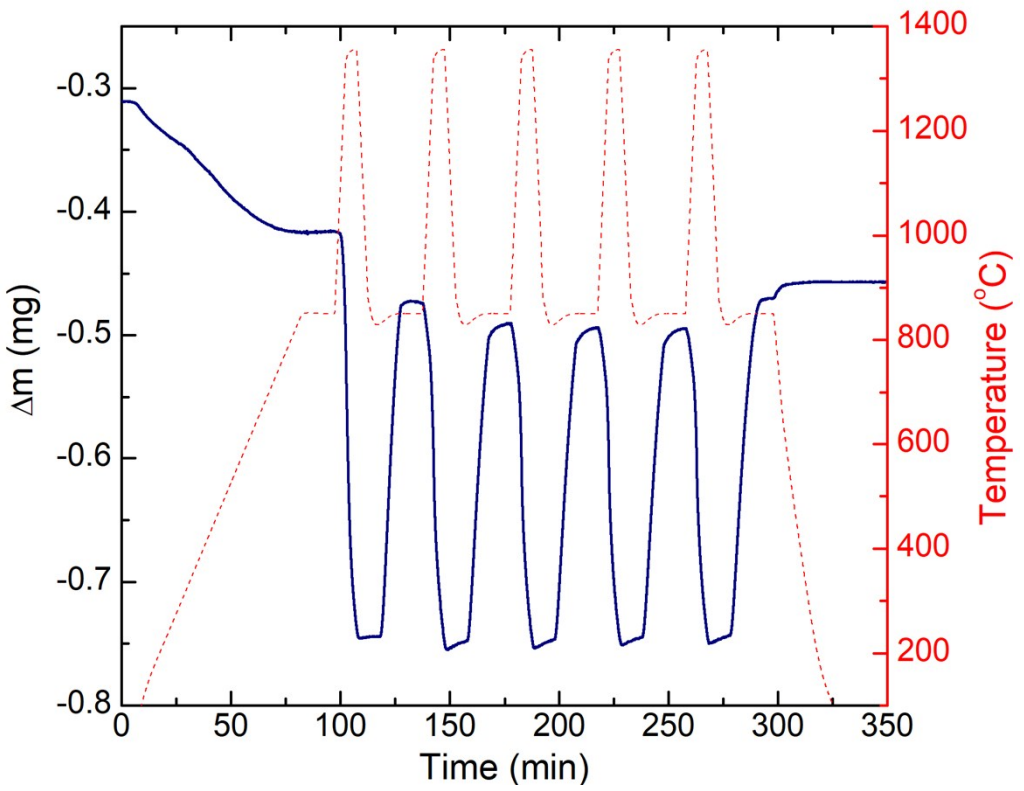

Figure S6 – 10H sample tested on 5 simulated WS cycles carried out in a TGA. The sample was heated at 10 °C /min to T_{OX} 850 °C in UHP N_2. The reduction step was done by heating the sample at 99 °C /min to T_{RE} 1350 °C and held for 330s. The sample was then cooled to T_{OX} at 99 °C /min and 16 sccm of synthetic air (21% O_2 balanced in N_2) mixed with 100 sccm of UHP N_2 was flowed for 10 min. The oxidizing flow was turned off and 100 sccm of UHP N_2 purged the chamber for another 10 min preparing the sample for the subsequent reduction cycle.

Figure S7 shows the XRD results on the 10*H* sample before and after the simulated run. Before TGA cycling, the sample presents only the 10*H* phase. However, after TGA cycle, the sample is converted entirely to the 12*R* phase. This demonstrates that under the SFR WS conditions used in this study, any reminiscent 10*H* phase is converted to the 12*R* phase.

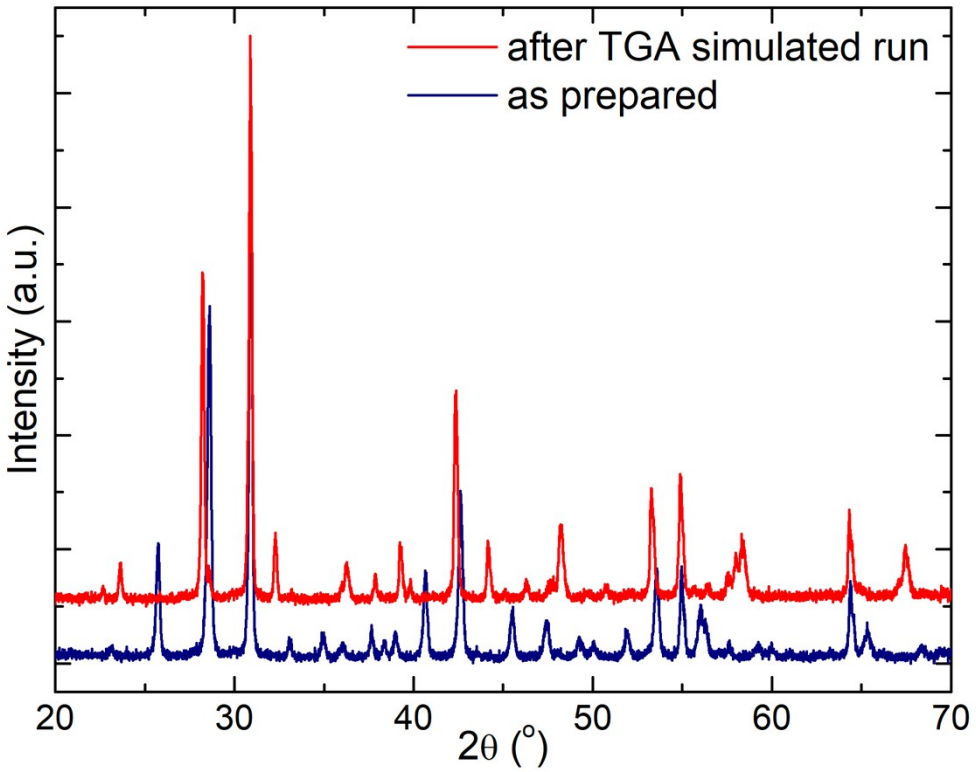

Figure S7 – XRD done on 10*H* samples before and after WS simulated runs done in TGA. The as prepared sample indicates the presence of 10*H* phase, whereas the sample after the TGA WS simulated run indicates that the 10*H* phase was converted to 12*R* phase.

References

1 A. M. Deml, V. Stevanović, C. L. Muhich, C. B. Musgrave and R. O'Hayre, *Energy Environ. Sci.*, 2014, **7**, 1996.

2 NRELMatDB, https://materials.nrel.gov.

3 R. Søndenå, S. Stølen, P. Ravindran, T. Grande and N. L. Allan, *Phys. Rev. B - Condens. Matter Mater. Phys.*, 2007, **75**, 1–10.

4 E. H. P. Cordfunke, A. S. Booij and M. E. Huntelaar, *J. Chem. Thermodyn.*, 1998, **30**, 437–447.

5 M. Aycibin, B. Erdinc and H. Akkus, *J. Electron. Mater.*, 2014, **43**, 4301–4307.

6 A. Le Gal, S. Ephane Abanades and G. Flamant, *Energy & Fuels*, 2011, **25**, 4836–4845.

7 S. Abanades, A. Legal, A. Cordier, G. Peraudeau, G. Flamant and A. Julbe, *J. Mater. Sci.*, 2010, **45**, 4163–4173.

8 N. Gokon, T. Suda and T. Kodama, *Thermochim. Acta*, 2015, **617**, 179–190.

9 A. H. McDaniel, A. Ambrosini, E. N. Coker, J. E. Miller, W. C. Chueh, R. O'Hayre and J. Tong, *Energy Procedia*, 2013, **49**, 2009–2018.

10 S. Zhai, J. Rojas, N. Ahlborg, K. Lim, M. Toney, H. Jin, W. C. Chueh and A. Majumdar, *Energy Environ. Sci.*, , DOI:10.1039/c8ee00050f.

11 A. H. McDaniel, E. C. Miller, D. Arifin, A. Ambrosini, E. N. Coker, R. O'Hayre, W. C. Chueh and J. Tong, *Energy Environ. Sci.*, 2013, **6**, 2424.

12 J. R. Scheffe, A. H. A. H. McDaniel, M. D. Allendorf and A. W. Weimer, *Energy Environ. Sci.*, 2013, **6**, 963–973.